Monotonicity of the Transfer Function for Eddy Current Tomography

Zhiyi Su, *Member, IEEE*, Lalita Udpa, *Life Fellow, IEEE*, and Antonello Tamburrino, *Senior Member, IEEE*

***Abstract*—Eddy current tomography (ECT) is a very well established electromagnetic nondestructive evaluation (NDE) method for the imaging of conducting and possibly magnetic materials. It relies on the capability of low-frequency electromagnetic fields to penetrate conducting materials. The underlying physical principle is electromagnetic induction, where the displacement current in Maxwell equations is neglected (magnetoquasistatic (MQS) limit). From a general perspective, ECT is an inverse problem, which poses serious challenges due to its inherent nonlinearity. This contribution introduces a transfer function for time-domain ECT, and proves that it satisfies the monotonicity principle (MP). This is relevant because MPs have been recognized as a key concept in developing real-time imaging methods and algorithms. The transfer function introduced in this contribution represents the input-output relationship for the forced response when the system is driven by an exponentially decaying current. Specifically, it corresponds to the Laplace transform of the system, evaluated on the real negative semiaxes. Finally, we describe the imaging method based on the MP, and we provide extensive 3-D numerical results in a realistic scenario, to demonstrate the effectiveness of the method.**

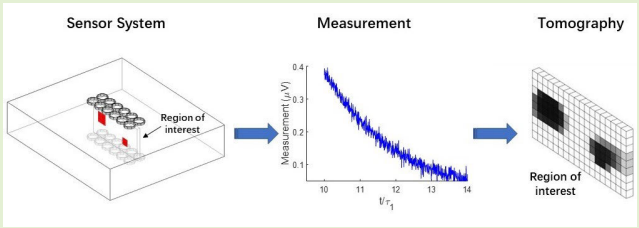

***Index Terms*— Eddy current tomography (ECT), imaging, inverse problems, monotonicity principles (MPs).**

I. Introduction

TOMOGRAPHY, or imaging, attempts to reconstruct the spatial distribution of material properties inside a specimen under testing, from externally measurable quantities. Usually, the measurement system applies excitation signals to the specimen to produce a measurable response.

Hard-field tomography, where the energy waves emitted from the source travel along straight lines regardless the material properties, as in the case of X-ray computed tomography (CT), magnetic resonance imaging (MRI), and positron emission tomography (PET), a well established and tractable inverse problem. The circumstance that the field lines are straight lines makes the imaging problem a linear problem, although ill-posed. On the contrary, in soft-field tomography, the shape of the field lines depends on the local value of the material properties, making the inverse problem nonlinear. In the case of eddy current tomography (ECT), the shape of the field lines of the induced electric current density strongly depends on the electrical conductivity and on the magnetic permeability, making it a nonlinear and strongly ill-posed inverse problem.

An operator satisfying the monotonicity principle (MP) provides a monotone relationships between the material properties and the measurable quantity. Although the first appearance of MP in the context of inverse problems dates back to 1990, in a work by Gisser et al. [1], it was in 2002 that Tamburrino and Rubinacci [2] recognized MP useful for solving inverse problems, in the application of electrical resistance tomography.

What makes tomography based on MP attractive, is that it is noniterative. MP methods and related algorithms are suitable for real-time imaging, can be easily parallelized, and can be implemented in low-power edge computation devices/platforms.

The approach based on the MP is among the few known noniterative methods suitable for soft-field imaging. In this class of imaging methods, Colton and Kirsch [3] introduced the first noniterative imaging algorithm, the linear sampling method (LSM), Kirsch [4] proposed the factorization method

Manuscript received 3 July 2023; revised 25 September 2023; accepted 26 September 2023. Date of publication 16 October 2023; date of current version 30 November 2023. The associate editor coordinating the review of this article and approving it for publication was Dr. Marko Vauhkonen. *(Corresponding author: Antonello Tamburrino.)*

Zhiyi Su is with the Zhejiang Laboratory, Hangzhou, Zhejiang 311121, China (e-mail: suzy@zhejianglab.edu.cn).

Lalita Udpa is with the Department of Electrical and Computer Engineering, Michigan State University, East Lansing, MI 48824 USA (e-mail: udpal@egr.msu.edu).

Antonello Tamburrino is with the Dipartimento di Ingegneria Elettrica e dell'Informazione "M. Scarano," Università degli Studi di Cassino e del Lazio Meridionale, 03043 Cassino, Italy (e-mail: antonello.tamburrino@unicas.it).

Digital Object Identifier 10.1109/JSEN.2023.3323304

(FM), Ikehata [5] proposed the enclosure method (EM) [6] and A. J. Devaney applied the well-known signal processing algorithm MUltiple SIgnal Classification (MUSIC) as an imaging method. Noniterative imaging methods have been mainly applied for solving the inverse obstacle problem, where one aims to reconstruct the shape of an anomaly in a known background material.

MP and related imaging algorithms have several desirable features. First, they are applicable without approximations even for real-world settings, in which the measurement systems are made by a finite number of sensors. This is not always the case in other methods, which are valid only when an infinite number of measurements is available. Second, under proper assumptions, it can be proved that a MP based method (MPM) provides upper and lower bounds for the unknown quantity [2], even in the presence of noise [7], [8]. Third, despite the fact that MPM was originally proved for stationary problems governed by an elliptic partial differential equation (PDE) see [1], [2], [9], [10] for electrical resistance, capacitance, and inductance tomography), they have been extended to a large variety of problems governed by different PDEs, such as: parabolic PDEs (see [11], [12], [13], [14], [15], [16] for ECT in several settings), hyperbolic PDEs (see [17] for microwave tomography, [18] for acoustic tomography, and [19] for optical tomography), nonlinear elliptic PDEs (see [20] for nonlinear electrical resistance tomography and [21] for nonlinear magnetic inductance tomography), and fractional Schrödinger equation [22], appearing in inverse problems when the domain under imaging is "probed" via an anomalous diffusion process more complex than the standard Brownian motion, modeled by the classical Laplacian. Fourth, MPM gives an exact reconstruction of the outer boundary of the unknown anomalous region, in the ideal setting of complete knowledge of the boundary measurement operator and noise free data [23]. MPM has also been applied to completely different contexts such as the homogenization of heterogeneous materials [24].

The first step in MP methods is to formulate a problem-specific operator, mapping the unknown quantity into the measured data, that satisfies the MP (see Section IV for details). In the magnetoquasistatic (MQS) regime and frequency domain operations, proper MP operators have been found for the small skin-depth [12], [25], [26] and large skin-depth approximations [11]. It is worth noting that the measured data in these two approximate regimes for the underlying parabolic PDE, is expressed by an elliptic PDE. This constitutes a potential drawback because it is known that the achievable spatial resolution increases, when moving from elliptic (static) to parabolic (quasi-static) to hyperbolic (wave propagation) phenomena. Therefore, with both small and large skin depth cases, this approach does not utilize the benefits of underlying physics of parabolic systems. One approach to overcome this drawback is to use measurements of a sequence of the time constants of the source-free response in pulsed ECT (PECT) [13], [14], [15], [16]. The operator giving the ordered sequence of the time constants satisfies a MP without relying on any approximation. Moreover, it is sensitive to the global spatial distribution of the material properties, with capabilities to image embedded interior anomalies. This latter feature is not trivial, since ECT is severely limited being a diffusive phenomenon. The drawback of this approach is that measuring the sequence of time constants is a highly ill-posed problem.

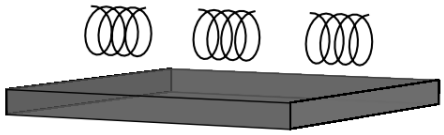

Fig. 1. Schematic of typical eddy current problem: a conducting domain and the probe made by an array of coils. The matrix of the current-to-voltage transfer functions at the coils of the system is the measured data.

The original contribution of this work is to recognize that the operator mapping the electrical resistivity of a conductor to the transfer matrix between coils of an array probing the specimen under testing, satisfies the MP. This MP is very effective because the transfer function can be easily measured, in practical PECT experiments. This new operator is expected to outperform MP for frequency domain ECT at both small or large skin-depth and MP for PECT.

The article is organized as follows. In Section II, the mathematical model for ECT is briefly summarized. In Section III, the transfer function is introduced and proved to be a MP operator. In Section IV, the imaging method based on the MP is implemented. In Section V, numerical examples in a real-world setting demonstrate the effectiveness of the imaging method. Finally, in Section VI, the conclusions are drawn.

II. Mathematical Model for ECT

The problem considered in this contribution consists of retrieving the shape of one or several anomalies located in the interior of a conductive domain Ω, by means of electromagnetic fields in the magnetoquasistatic limit, where the displacement current is negligible [27]. A relevant case of interest is that of ECT, where the interest is in finding defects in an otherwise homogeneous material [28], [29].

The conducting domain is assumed to be nonmagnetic, although the approach can be extended to conductors with linear magnetic properties. We consider the typical case of a conductive domain Ω which is surrounded by an isolating material and, therefore, the normal component of the eddy current density $\mathbf{J}$ on the surface of the sample Ω is vanishing.

The probing system for ECT is made by an array of N_c coils exterior to the conducting domain (see Fig. 1). The N_c coils of the array are used both as excitation and pick-up. Time-varying currents $i_1(t), \ldots, i_{N_c}(t)$ are impressed in these coils, and the corresponding induced voltages $v_1(t), \ldots, v_{N_c}(t)$, across the same set of coils, are measured.

The anomalous region V, which is made by one or multiple defects of arbitrary topology and shape, has a resistivity different from that of the background, i.e., the conducting domain Ω. Retrieving the shape of one or more anomalies is an inverse obstacle problem.

We highlight that the proposed approach is even more general, and includes nonhomogeneous materials, as well as anisotropic conductors.

A. Mathematical Model

The variational formulation (with respect to the spatial coordinates) for the eddy current problem is [30]

$$\begin{aligned}\int_\Omega \mathbf{J}'(\mathbf{r})\cdot\eta\mathbf{J}(\mathbf{r},t)\mathrm{d}V &= -\partial_t\int_\Omega \mathbf{J}'(\mathbf{r})\cdot\mathcal{A}_i[\mathbf{J}(\cdot,t)]\mathrm{d}V \\ &\quad -\partial_t\int_\Omega \mathbf{J}'(\mathbf{r})\cdot\mathbf{A}_c(\mathbf{r},t)\mathrm{d}V \quad \forall\mathbf{J}'\in H_L(\Omega) \end{aligned} \tag{1}$$

where $\mathbf{J}\in L^2(0,T;H_L(\Omega))$, the functional space $H_L(\Omega)$ is defined as

$$H_L(\Omega)=\left\{\mathbf{v}\in H(\mathrm{div};\Omega)|\nabla\cdot\mathbf{v}=0,\mathbf{v}\cdot\hat{n}=0 \text{ on } \partial\Omega\right\} \tag{2}$$

η is the point-wise resistivity, $\mathcal{A}_i[\cdot]$ is an integral operator acting on the spatial coordinates only

$$\mathcal{A}_i:\mathbf{v}(\mathbf{r})\in H_L(\Omega)\rightarrow\frac{\mu_0}{4\pi}\int_\Omega\frac{\mathbf{v}(\mathbf{r})}{\|\mathbf{r}-\mathbf{r}'\|}\mathrm{d}V\in L^2\left(\Omega;\mathbb{R}^3\right) \tag{3}$$

and $\mathbf{A}_c$ is the magnetic vector potential due to the assigned driving currents.

When the driving system is made by a proper set of N_c filamentary coils, $\mathbf{A}_c$ can be expressed as

$$\mathbf{A}_c(\mathbf{r},t)=\sum_{k=1}^{N_c}\mathbf{A}_{c,k}(\mathbf{r})i_k(t) \tag{4}$$

where $i_k(\cdot)$ is the electrical current prescribed at the kth coil, $\mathbf{A}_{c,k}$ is the vector potential due to an unitary current flowing in the kth coil, that is given by

$$\mathbf{A}_{c,k}(\mathbf{r})=\frac{\mu_0}{4\pi}\int_{\gamma_k}\frac{\mathrm{d}\mathbf{l}'}{\|\mathbf{r}-\mathbf{r}'\|}, \tag{5}$$

γ_k being the curve representing the path of the kth coil. In this case, the integral appearing at the right hand side of (1) is

$$\int_\Omega\mathbf{J}'(\mathbf{r})\cdot\mathbf{A}_c(\mathbf{r},t)\mathrm{d}V=\sum_{k=1}^{N_c}\left[\int_\Omega\mathbf{J}'(\mathbf{r})\cdot\mathbf{A}_{c,k}(\mathbf{r})\mathrm{d}V\right]i_k(t). \tag{6}$$

The voltage induced by the eddy currents at the kth coil is

$$v_k=\frac{\mathrm{d}\phi_k^{\mathrm{eddy}}}{\mathrm{d}t} \tag{7}$$

where the linked-flux ϕ_k^{eddy} due to the eddy currents is

$$\begin{aligned}\phi_k^{\mathrm{eddy}}(t)&=\int_{\gamma_k}\frac{\mu_0}{4\pi}\int_\Omega\frac{\mathbf{J}(\mathbf{r},t)}{\|\mathbf{r}-\mathbf{r}'\|}\mathrm{d}V\cdot\mathrm{d}\mathbf{l}' \\ &=\int_\Omega\mathbf{J}(\mathbf{r},t)\cdot\mathbf{A}_{c,k}(\mathbf{r})\mathrm{d}V.\end{aligned} \tag{8}$$

B. Numerical Model

The numerical model (see [31], [32]) is obtained by introducing the electric vector potential $\mathbf{T}$ ($\mathbf{J}=\nabla\times\mathbf{T}$) to enforce $\nabla\cdot\mathbf{J}=0$, and expanding $\mathbf{T}$ by means of edge-element shape functions $\mathbf{N}_i's$ (see [33]), i.e.,

$$\mathbf{T}(\mathbf{r},t)=\sum_{i=1}^{N}T_i(t)\mathbf{N}_i(\mathbf{r}) \tag{9}$$

where N is the number of degrees of freedom (DoFs) in the discrete model. The tree-cotree decomposition technique is used to impose both the uniqueness (gauge condition) of the electric vector potential and the boundary condition $\mathbf{J}\cdot\hat{\mathbf{n}}=0$ on $\partial\Omega$ [32], [34], [35].

The Galerkin method applied to (1) yields the linear system

$$\left(\mathbf{R}+\frac{\mathrm{d}}{\mathrm{d}t}\mathbf{L}\right)\mathbf{T}(t)=\mathbf{s}(t) \tag{10}$$

where the elements of matrices $\mathbf{R}$ and $\mathbf{L}$ and vector $\mathbf{s}$ are given by (see [11], [14])

$$R_{ij}\triangleq\int_\Omega\nabla\times\mathbf{N}_i\cdot\eta\nabla\times\mathbf{N}_j\mathrm{d}V \tag{11}$$

$$L_{ij}\triangleq\frac{\mu_0}{4\pi}\int_\Omega\int_\Omega\frac{\nabla\times\mathbf{N}_i(\mathbf{r})\cdot\nabla\times\mathbf{N}_j(\mathbf{r}')}{\|\mathbf{r}-\mathbf{r}'\|}\mathrm{d}V\mathrm{d}V' \tag{12}$$

$$s_i(t)\triangleq-\frac{\mathrm{d}}{\mathrm{d}t}\int_\Omega\nabla\times\mathbf{N}_i(\mathbf{r})\cdot\mathbf{A}_c(\mathbf{r},t)\mathrm{d}V. \tag{13}$$

When the driving system is made by a proper set of N_c coils, as in this article, we have that

$$\mathbf{s}(t)=-\mathbf{M}\frac{\mathrm{d}\mathbf{i}(t)}{\mathrm{d}t} \tag{14}$$

where $\mathbf{i}$ is the $N_c\times 1$ column vector of the coil currents $i_k s$. The voltages due to eddy currents across the set of coils are given by

$$\mathbf{v}(t)=\mathbf{M}^T\frac{\mathrm{d}\mathbf{T}(t)}{\mathrm{d}t} \tag{15}$$

where $M_{ik}=\int_\Omega\nabla\times\mathbf{N}_i(\mathbf{r})\cdot\mathbf{A}_{c,k}(\mathbf{r})\mathrm{d}V$ and $\mathbf{v}$ is the $N_c\times 1$ column vector of the coil voltages.

III. Monotonicity of Transfer Function

In this section, we first introduce the concept of transfer function in this specific setting and, then, we prove that the operator mapping the material property into the transfer function satisfies a MP.

A. Definition of Transfer Function

Let us assume the input current is exponentially decaying after time $t=0$, i.e.,

$$\mathbf{i}(t)=\mathbf{i}_0 1(t)\mathrm{e}^{-t/\tau}+\mathbf{i}_0 1(-t) \tag{16}$$

where $\mathbf{i}_0$ is a vector describing the magnitude of currents injected in the coil array, τ is a prescribed positive constant, and $1(t)$ is the Heaviside step function

$$1(t)=\begin{cases}0, & t<0\\ \frac{1}{2}, & t=0\\ 1, & t>0.\end{cases} \tag{17}$$

An illustration of the current waveform is given in Fig. 2.

The solution to (10), given the prescribed source in (16) consists of two parts, a source-free response and a forced response

$$\mathbf{T}(t)=\mathbf{T}^{\mathrm{free}}(t)+\mathbf{T}^{\mathrm{forced}}(t). \tag{18}$$

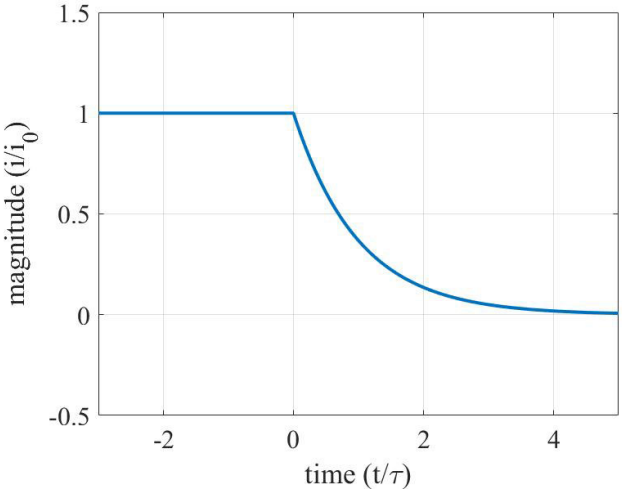

Fig. 2. Example of the excitation waveform.

The source free response is the solution for the homogeneous problem, and can be expressed as superposition of natural modes [14]

$$\mathbf{T}^{\text{free}}(t) = \sum_{k=1}^{N} c_k \mathbf{u}_k \mathrm{e}^{-t/\tau_k} \tag{19}$$

where the time constants $\tau_1 \geq \tau_2 \geq \cdots \geq \tau_N > 0$ are bounded, and the $\mathbf{u}_k s$ are the corresponding modes. Time constants and related modes are an intrinsic property of the test sample, depending on η and Ω and not depending on the excitation. Specifically, the time constants τ_k and the related modes $\mathbf{u}_k$ are the generalized eigenvalues and eigenvectors of the following problem (see [14]):

$$\mathbf{L}\mathbf{u} = \tilde{\tau}\mathbf{R}\mathbf{u}. \tag{20}$$

Moreover, it can be proved that when $N \to +\infty$ expansion (19) is still valid, the time constants form a bounded and nonnegative sequence which approaches 0 asymptotically (see [13]).

The induced voltage corresponding to the solution of the homogeneous equation is

$$\begin{aligned}\mathbf{v}^{\text{free}}(t) &= \mathbf{M}^T \frac{\mathrm{d}\mathbf{T}^{\text{free}}(t)}{\mathrm{d}t} \\ &= -\sum_{k=1}^{N} c_k \mathbf{M}^T \mathbf{u}_k \frac{\mathrm{e}^{-t/\tau_k}}{\tau_k}.\end{aligned} \tag{21}$$

The forced response satisfies

$$\left(\mathbf{R} + \frac{\mathrm{d}}{\mathrm{d}t}\mathbf{L}\right) \mathbf{T}^{\text{forced}}(t) = -\mathbf{M}\frac{\mathrm{d}}{\mathrm{d}t}\mathbf{i}_0 \mathrm{e}^{-t/\tau} \tag{22}$$

and it can be found assuming $\mathbf{T}^{\text{forced}}(t) = \mathbf{A}\mathrm{e}^{-t/\tau}$. Specifically, by plugging the previous expression into (22), we found that

$$\mathbf{A} = (\tau\mathbf{R} - \mathbf{L})^{-1}\mathbf{M}\mathbf{i}_0. \tag{23}$$

Substituting the expression for $\mathbf{T}^{\text{forced}}$ into (15), we have

$$\mathbf{v}^{\text{forced}}(t) = \mathbf{Z}\mathbf{i}_0 \mathrm{e}^{-t/\tau} \tag{24}$$

where

$$\mathbf{Z} = -\frac{1}{\tau}\mathbf{M}^T(\tau\mathbf{R} - \mathbf{L})^{-1}\mathbf{M}. \tag{25}$$

Summing up, under the assumption of an exponentially decaying current $\mathbf{i}(t) = \mathbf{i}_0 \mathrm{e}^{-t/\tau}$ for $t > 0$, we have that the output voltage is given by

$$\mathbf{v}(t) = \mathbf{Z}\mathbf{i}(t) + \mathcal{O}\left(\mathrm{e}^{-t/\tau_1}\right), \quad t > 0. \tag{26}$$

Matrix $\mathbf{Z}$ plays a key role. Specifically, it gives the input-output relationship for the forced response, under an exponentially decaying input current, as it appears from (24) and (26).

Remark 1: Although not required in this work, we highlight that the computation of coefficients $c_k s$ in (19) can be easily carried out by imposing $\mathbf{T}(0) = \mathbf{0}$. Indeed, before the transient is started at time $t = 0$, the eddy current density is vanishing, therefore $\mathbf{T}(t) = \mathbf{0}$ for $t < 0$. Specifically, we have $\mathbf{c} = -\mathbf{U}^{-1}\mathbf{A}$, being $\mathbf{c} = [c_1, \ldots, c_N]^T$ and $\mathbf{U} = [\mathbf{u}_1, \ldots, \mathbf{u}_N]$.

B. Connection to the Laplace Transform

Matrix $\mathbf{Z}$ is the current-to-voltage transfer function at the coils of the system, evaluated on the real negative axis at $p = -1/\tau$. In fact, applying the Laplace transform to (10), (14), and (15) with $\mathbf{T}(0) = \mathbf{0}$, we have

$$(\mathbf{R} + p\mathbf{L})\mathbf{T}(p) = -p\mathbf{M}\mathbf{i}(p) \tag{27}$$

$$\mathbf{v}(p) = p\mathbf{M}^T\mathbf{T}(p) \tag{28}$$

where $\mathbf{i}(p)$, $\mathbf{v}(p)$, and $\mathbf{T}(p)$ are the Laplace transforms of $\mathbf{i}(t)$, $\mathbf{v}(t)$, and $\mathbf{T}(t)$, respectively, evaluated at the complex value p.

From (27) and (28), it turns out that

$$\mathbf{v}(p) = \mathbf{H}(p)\mathbf{i}(p) \tag{29}$$

where $\mathbf{H}(p) = -p^2\mathbf{M}^T(\mathbf{R} + p\mathbf{L})^{-1}\mathbf{M}$ is the transfer function. Therefore, $\mathbf{Z} = \mathbf{H}(p = -1/\tau)$.

As it is well known, this transfer function exists for any complex p with real part greater that $-1/\tau_1$. Therefore, we have the constraint that τ has to be greater than τ_1. From the physical standpoint, $\tau > \tau_1$ guarantees that the $\mathbf{Z}\mathbf{i}(t)$ is the leading term in (26), for large enough t.

C. Measurement of the Transfer Function

In principle, the step-by-step derivation of $\mathbf{Z}$ presented in Section III-A may be replaced by the direct derivation of the transfer function presented in Section III-B. Despite this, the derivation of Section III-A is useful for deriving the expression for the response as seen in (26) in the time-domain which, in turn, is required to develop a method to extract the transfer function $\mathbf{Z}$ from measured data.

The measurement of the elements of the transfer function $\mathbf{Z}$ following (26) is, in principle, straightforward. The elements of $\mathbf{Z}$ are the self/mutual impedances relating the forced response for the output voltage to the input current, for large t. To estimate $\mathbf{Z}$, one may choose $\tau > \tau_1$ and measure the pick-up coil voltages for t large enough so that the source free response is negligible with respect to the forced response. This condition is met when $t/\tau \gg (\tau/\tau_1 - 1)^{-1}$ as it follows

from (26) written as $Z_{lk} = v_l(t)/i_k(t) + \mathcal{O}(\mathrm{e}^{-(t/\tau)((\tau/\tau_1)-1)})$, being $i_n = 0$ for $n \neq k$.

In practice, the noise affects the measurements. Therefore, the measurement of the $Z_{lk}s$ requires a slightly more sophisticated approach. Hereafter, we assume that: 1) the coil currents are imposed whereas the coil voltages are measured; 2) the noise level affecting the imposed currents is negligible if compared to the noise level affecting the measured voltages; and 3) the noise affecting the measured voltage $\tilde{v}_l$ is additive, that is

$$\tilde{v}_l(t) = v_l(t) + n_l(t) \tag{30}$$

$$= Z_{lk} i_k(t) + n_l(t) + \mathcal{O}\left(\mathrm{e}^{-t/\tau_1}\right). \tag{31}$$

Then, Z_{lk} is estimated from noisy data as the minimizer of the functional $\Phi(z) = \int_{T_1}^{T_2} |\tilde{v}_l(t) - z i_k(t)|^2 \mathrm{d}t$ (least square approach). In this way, the estimate of Z_{lk} is

$$\tilde{Z}_{lk} = \frac{\int_{T_1}^{T_2} \tilde{v}_l(t)\mathrm{d}t}{\int_{T_1}^{T_2} i_k(t)\mathrm{d}t}, \quad l,\ k = 1, 2, \ldots, N_c \tag{32}$$

where $i_k(t) = i_0 \mathrm{e}^{-t/\tau}$ and $i_n(t) = 0$ for $n \neq k$, for $t > 0$. In (32), T_1 and T_2 have to be properly chosen (see Section V).

D. MP for the Transfer Function

Here, we describe the key MP at the foundation of the imaging method.

Let $\Omega \subset \mathbb{R}^3$ be a conductive and nonmagnetic domain, and let η_α and η_β two electrical conductivities defined in Ω. We define $\mathbf{Z}_\alpha$ and $\mathbf{Z}_\beta$ to be the transfer matrices related to η_α and η_β, respectively. Similarly, we define τ_1^α and τ_1^β to be the largest time constants for η_α and η_β, respectively. We have the following Theorem.

Theorem 1: Let $\Omega \subset \mathbb{R}^3$ be a conductive and nonmagnetic domain and let η_α and η_β be two electrical resistivities defined in Ω. It results that

$$0 < c \leq \eta_\alpha \leq \eta_\beta \text{ in } \Omega \Rightarrow \mathbf{Z}_\alpha \preceq \mathbf{Z}_\beta \tag{33}$$

where c is a proper constant, $\tau > \tau_1^\alpha$, $\tau > \tau_1^\beta$, and $\eta_\alpha \leq \eta_\beta$ means that $\eta_\alpha(\mathbf{r}) \leq \eta_\beta(\mathbf{r})$, for almost everywhere $\mathbf{r} \in \Omega$ and $\mathbf{Z}_\alpha \preceq \mathbf{Z}_\beta$ means that $\mathbf{Z}_\alpha - \mathbf{Z}_\beta$ is a negative semidefinite matrix.

Proof: From $\eta_\alpha \leq \eta_\beta$ and the definition of matrix $\mathbf{R}$ in (11), it turns out that $\mathbf{R}_\alpha \preceq \mathbf{R}_\beta$ (see also [11]). Then, we have that

$$\mathbf{R}_\alpha \preceq \mathbf{R}_\beta \Leftrightarrow (\tau\mathbf{R}_\alpha - \mathbf{L}) \preceq (\tau\mathbf{R}_\beta - \mathbf{L}) \tag{34}$$

$$\Leftrightarrow (\tau\mathbf{R}_\alpha - \mathbf{L})^{-1} \succeq (\tau\mathbf{R}_\beta - \mathbf{L})^{-1}. \tag{35}$$

Proposition at the right hand side of (35) implies ($\Rightarrow$) that

$$\begin{aligned} &\mathbf{M}^T(\tau\mathbf{R}_\alpha - \mathbf{L})^{-1}\mathbf{M} \succeq \mathbf{M}^T(\tau\mathbf{R}_\beta - \mathbf{L})^{-1}\mathbf{M} \\ &\Leftrightarrow -\frac{1}{\tau}\mathbf{M}^T(\tau\mathbf{R}_\alpha - \mathbf{L})^{-1}\mathbf{M} \preceq -\frac{1}{\tau}\mathbf{M}^T(\tau\mathbf{R}_\beta - \mathbf{L})^{-1}\mathbf{M} \\ &\Leftrightarrow \mathbf{Z}_\alpha \preceq \mathbf{Z}_\beta \end{aligned} \tag{36}$$

and, therefore, (33) holds.

Remark 2: Equation (35) holds if matrices $\tau\mathbf{R}_\alpha - \mathbf{L}$ and $\tau\mathbf{R}_\beta - \mathbf{L}$ are positive definite. This is the case when $\tau > \tau_1^\alpha$ and $\tau > \tau_1^\beta$, as in the assumptions of Theorem 1.

E. MP for the Inverse Obstacle Problem

MP (33) of Theorem 1 is in a very general form. It can be conveniently specialized when the electrical resistivity assumes two different values, $\eta_0 > 0$ for the background material and $\eta_i > 0$ for an inclusion occupying region $V \subset \Omega$, and the interest is in reconstructing the shape (inverse obstacle problem) of V. The first successful specializations of MP to this inverse obstacle problem can be found in [2].

The spatial distribution of the electrical resistivity in Ω relative to the presence of the anomaly V is

$$\eta_V(\mathbf{r}) = \begin{cases} \eta_i, & \text{in } V \\ \eta_0, & \text{in } \Omega \backslash V. \end{cases} \tag{37}$$

Hereafter, we assume that $\eta_i > \eta_0$, the typical case in nondestructive testing of conducting materials. We have the following theorem.

Theorem 2: Let $\Omega \subset \mathbb{R}^3$ be a conductive and nonmagnetic domain and let $D_\alpha \subset \Omega$ and $D_\beta \subset \Omega$ be two domains representing inclusions in Ω. It results that

$$D_\alpha \subseteq D_\beta \subset \Omega \Rightarrow \mathbf{Z}_\alpha \preceq \mathbf{Z}_\beta \tag{38}$$

where $\mathbf{Z}_\alpha$ and $\mathbf{Z}_\beta$, are the transfer matrices related D_α and D_β, and $\tau > \tau_1^\alpha$, $\tau > \tau_1^\beta$.

Proof: The proof is trivial by recognizing that $D_\alpha \subseteq D_\beta$ implies that $\eta_{D_\alpha} \leq \eta_{D_\beta}$ and applying Theorem 1.

Remark 3: It is worth noting that the electrical resistivity in the background and/or in the inclusion do not need to be constant. Theorem 2 and (38) are valid even if $\eta_0 = \eta_0(\mathbf{r})$ and $\eta_i = \eta_i(\mathbf{r})$, as long as $\eta_0(\mathbf{r}) \leq \eta_i(\mathbf{r})$, for almost everywhere $\mathbf{r} \in \Omega$.

IV. Noniterative Imaging via Monotonicity

In this section, we shortly summarize the imaging method for the inverse obstacle problem.

The key idea is that (38) is equivalent to $\mathbf{Z}_\alpha \not\preceq \mathbf{Z}_\beta \Rightarrow D_\alpha \not\subseteq D_\beta$. Therefore, if D_α is equal to a known set $T \subseteq \Omega$ and D_β is equal to the unknown domain V, then condition $\mathbf{Z}_T \not\preceq \mathbf{Z}_V$ implies that $T \not\subseteq V$. In other terms, from the measured data, it is possible to infer if the prescribed set T is not included in V. By repeating this test for several/many sets T located in different positions, it is possible to estimate the shape of V. We refer to [2], [11], and [14] for details.

A. Imaging Algorithm

MP for the transfer function can be exploited to formulate a noniterative imaging algorithm. Let $\{T_j\}_{j=1}^P$, be a set of small volumetric domains located in the sample. The $T_j s$ are termed as test elements, selected such that their union covers the region of interest (ROI), where one is looking for anomalies.

Let V be the unknown anomaly. From (38), if $T_j \subseteq V$, then, matrix $\mathbf{Z}_{T_j} - \mathbf{Z}_V$ is negative semidefinite. Vice versa, if matrix $\mathbf{Z}_{T_j} - \mathbf{Z}_V$ is not negative semidefinite, then, T_j is surely not contained in V. Therefore, we may estimate V as follows:

$$V_U = \bigcup \{T_j | \mathbf{Z}_{T_j} \preceq \mathbf{Z}_V\}. \tag{39}$$

In this case, the unknown anomaly is approximated by the union of test elements that appear to be part of the anomaly, from the monotonicity test. Another reconstruction formula can be easily obtained exploiting test elements that appear to be larger than the unknown anomaly, from the monotonicity test. In this case, we estimate V as follows:

$$V_L = \bigcap \{T_j | \mathbf{Z}_{T_j} \succeq \mathbf{Z}_V\}. \tag{40}$$

The reconstruction is sought as intersection of test elements appearing to contain the unknown anomalous region V.

B. Computational Cost

The proposed method has a very low computational cost, as it involves only a trivial test on the sign of the eigenvalues of each difference matrix $\mathbf{Z}_{T_j} - \mathbf{Z}_V$, with dimension equal to the number of coils of the probing array. In practical systems, this number does not exceed the hundreds. To retrieve the estimate of the unknown anomaly V, i.e., V_L and/or V_U, one needs to repeat this simple test for all test elements. The total number of test elements is predefined by the inspector and it depends on the desired spatial resolution.

Summing up, the computational cost for forming the reconstruction with either (39) or (40), is equal to $\mathcal{O}(PN_c^3)$, where P is the total number of test domains and N_c^3 comes from the effort to compute the eigenvalues of an $N_c \times N_c$ matrix. This estimate gives the total computational cost for processing the measured data $\mathbf{Z}_V$. It is linear with respect to P, which is related to the spatial resolution, making it suitable for real-time imaging.

The $\mathcal{O}(PN_c^3)$ estimate of the computational cost does not take into account the time required for getting the test matrices $\mathbf{Z}_{T_j}s$. It is worth noting the test matrices can be either computed numerically or evaluated experimentally. This task needs to be done only once. Indeed, the computation of the test matrices $\mathbf{Z}_{T_j}s$ does not depend on the measured data to be processed. Therefore, the test matrices can be precomputed once for all: they depend on the specific driving system and the geometries and material properties of the specimen and the test domains. Moreover, both the numerical computation or the experimental measurement of the set of test matrices $\mathbf{Z}_{T_j}s$ can be carried out in parallel.

C. Noise and Bounds

In practice, due to the presence of the noise, only a noisy realization $\tilde{\mathbf{Z}}_V$ is available. In line with [8], if an upper bound δ to the two-norm of the noise matrix $\mathbf{N}$ is known, then $\|\tilde{\mathbf{Z}}_V - \mathbf{Z}_V\|_2 \leq \delta$ and

$$\tilde{\mathbf{Z}}_V - \delta\mathbf{I} \leq \mathbf{Z}_V \leq \tilde{\mathbf{Z}}_V + \delta\mathbf{I}. \tag{41}$$

In this case, the unknown anomaly can be estimated as

$$V_U = \bigcup \{T_j | \mathbf{Z}_{T_j} \leq \tilde{\mathbf{Z}}_V + \delta\mathbf{I}\}. \tag{42}$$

and

$$V_L = \bigcap \{T_j | \mathbf{Z}_{T_j} \geq \tilde{\mathbf{Z}}_V - \delta\mathbf{I}\}. \tag{43}$$

We highlight that (39) and (40) correspond to (42) and (43), in the absence of noise, i.e., for $\delta = 0$.

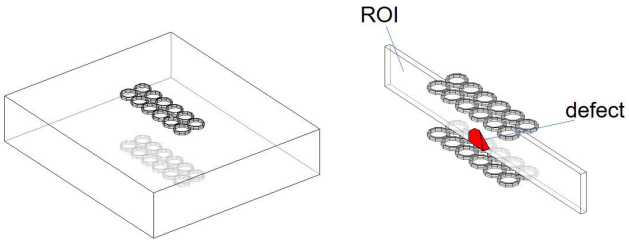

Fig. 3. Test specimen and the probing system made by two arrays of 12 coils (left). ROI, together with a defect (red) and the probing system (right).

It is worth noting that but under proper assumptions (see [2], [7], [8]) and even in the presence of noise, it results

$$V_L \subseteq V \subseteq V_U. \tag{44}$$

V. Application Case

In this section, an application of the theory of defect imaging via MP of transfer function is presented. The experimental validation is outside the scope of this contribution and will be part of a future study. In this article, we provide the theoretical framework, the data processing (imaging) method, and a first numerical feasibility study to validate it.

In the following, we first describe the problem of the inspection of a metallic plate via eddy current nondestructive evaluation (NDE), then, we describe all the steps involved in the imaging process, providing detailed examples of reconstructions for different defects. It is worth noting that the inspection of a metallic plate represents a relevant configuration in eddy current NDE, which is found in many practical applications.

The specimen under inspection is an Aluminum plate of 12 cm $\times$ 14 cm $\times$ 3 cm. The objective of the imaging process is to recover the shape of an unknown defect(s) which may be present in the specimen. Without loss of generality, we assume that the crack is confined in a known ROI, which is one vertical slice of the specimen. The electrical conductivity of the specimen is 3.7×10^7 S/m, whereas that of the defect is negligible, relative to the background conductivity. The geometry of the configuration is shown in Fig. 3. The probing system consists of two arrays of coils, located on both sides of the Aluminum plate. The lift-off distance between the coils and the plate is 1 mm. The total number of coils is 24 (12 per each array) and all coils in the arrays are identical (100 turns, inner diameter of 8 mm and outer diameter of 10 mm). The design of the probing system in the framework of MP is nontrivial (see [36], for instance).

Other than the 2×12 elements array, arrays of 24 elements and 12 elements placed on the top of the plate have been considered for performances comparisons (see Fig. 4).

In order to demonstrate the effectiveness of our imaging method, results for two families of defects are considered. The first family consists of three "canonical" cases covering typical eddy current NDE configurations encountered in industrial applications. The second family of defects consists of "complex" geometries designed to define the limitations of the method, are less common in practical cases. The first family consists of three different defects, showed in Fig. 5: a

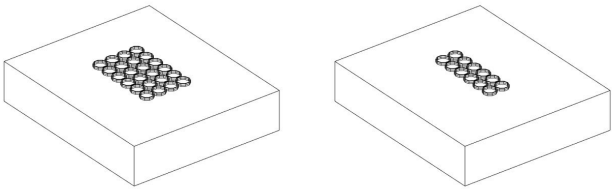

Fig. 4. Test specimen and the probing system made by one arrays of 24 coils (left). Test specimen and the probing system made by one arrays of 12 coils (right).

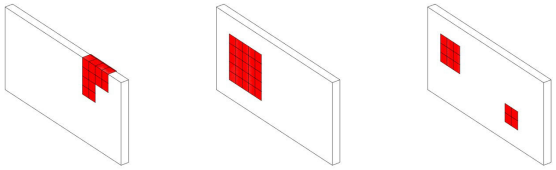

Fig. 5. Canonical defects to be imaged. Surface breaking defect (left). Buried defect (center). Multiple defect (right).

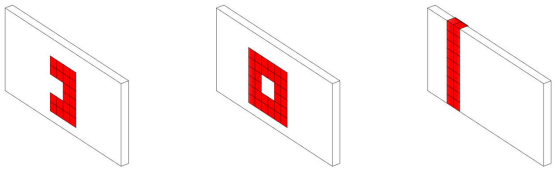

Fig. 6. Complex defects to be imaged. Nonconvex defect (left). Nonsimply connected defect (center). Through hole defect (right).

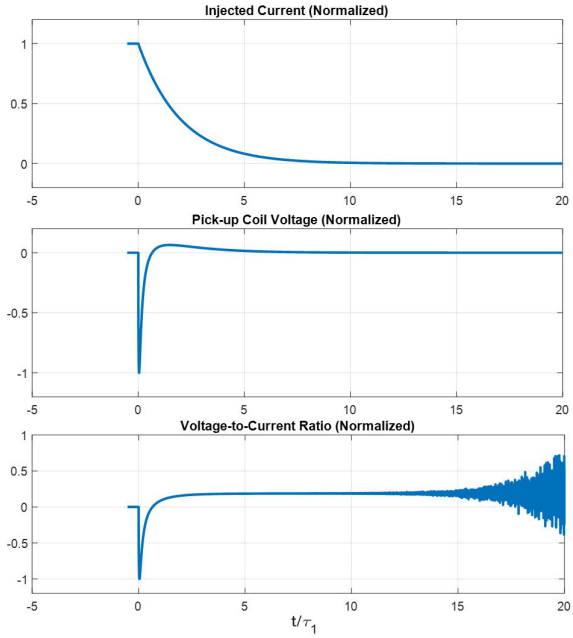

Fig. 7. Time domain waveforms.

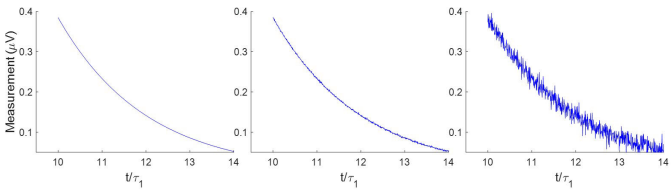

Fig. 8. Noise corrupted measurements at various noise level. $\eta = 10^{-5}$ (left), $\eta = 10^{-4}$ (middle), and $\eta = 10^{-3}$ (right).

surface breaking defect, a buried defect, and two interacting defects. These cases cover different aspects: a surface breaking defect (Fig. 5, left) is easier to be detected/imaged than a buried defect (Fig. 5, center) because of the diffusive nature of quasi-static fields, whereas interacting defects (Fig. 5, right) pose challenges with regards to the spatial resolution and, in some imaging methods, they cannot be reconstructed. The second family (see Fig. 6) consists of three different defects: a nonconvex defect (Fig. 6, left), a nonsimply connected defect (Fig. 6, center) and a through hole defect (Fig. 6, right). The first two defects test the capability of the eddy current NDE system to resolve details of the shape of the unknown defect, whereas the third geometry tests the system performances on defects making the ROI topologically disconnected.

As discussed in Section III-A, to extract the transfer function $\mathbf{Z}$ from time-domain measurements, the excitation current has to be exponentially decaying. Following [14], the time constants of the natural response are evaluated by solving the generalized eigenvalue problem (20). In this example, the largest time constant is $\tau_1 = 12.6$ ms. The time constant τ for the input current is chosen twice this value, i.e., $\tau = 25.2$ ms.

Fig. 7 provides an illustration of the main waveforms: the excitation current, the pick-up voltage, and their ratio. The plot of the waveform of the ratio, which asymptotically gives the sought element of the transfer function, shows that retrieving its limiting value in the presence of noise is nontrivial. The selection of T_1 and T_2 in (32) is carried out to meet two conditions: on one hand, T_1 and T_2 should be large enough such that $t/\tau \gg (\tau/\tau_1 - 1)^{-1}$ for any $t \in [T_1, T_2]$; on the other hand, T_1 and T_2 should not to be too large, to get the estimate of the limiting value overwhelmed by the measurement noise. After extensive numerical simulations, we found that $T_1 = 0.126$ s and $T_2 = 0.176$ s constitute values that satisfy the two aforementioned conditions.

The noise signal $n_l(t)$ is due to the measurement system. Usually, in a properly designed and calibrated system, it can be considered as a Gaussian noise with mean $\mu = 0$ and standard variation σ proportional to the scale of the signal. In this example, we assume $\sigma = \eta v_l|_{t=3\tau_1}$, being η a constant parameter representing the noise level. Fig. 8 shows an example of noisy measurement, zoomed in between T_1 and T_2, at various noise levels $\eta = 10^{-5}$, 10^{-4}, and 10^{-3}. This noise level can be translated into the well-known signal-to-noise ratio, or SNR, defined as

$$\mathrm{SNR} = 10 \log_{10} \frac{\int_{T_1}^{T_2} v^2(t) \mathrm{d}t}{\int_{T_1}^{T_2} n^2(t) \mathrm{d}t}.$$

In this way, we can easily establish a correspondence between η and the SNR, as shown in Table I.

As imaging method based on the MP of the transfer function, we use a union-based scheme of (42). The selection of the geometry (size, shape, and topology) of test elements is another relevant aspect to achieve accurate reconstructions. As a rule of thumb, one may choose the size of a test element of the order of the expected spatial resolution. If the dimension of a test element is too small, the occurrence of false positives

TABLE I
NOISE LEVEL η AND THE CORRESPONDING SNR

η	SNR
10^{-5}	63.5
10^{-4}	43.5
10^{-3}	23.5

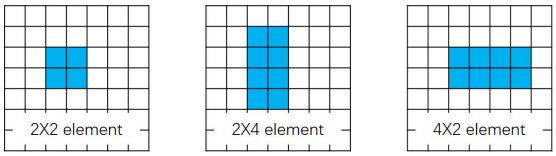

Fig. 9. Three different types of test elements for the imaging method. Each test elements generate a family of test elements by horizontal and/or vertical translations of one single pixel.

increases. On the other hand, if the dimension of a test element is too large, details of the defect which cannot be represented via union of test element contained in the unknown defect, can be missed. Or, even worse, if the defect is smaller than the test elements, it can go undetected.

The family of test elements needs only to be a covering of the ROI, i.e., the union of all test elements covers the ROI. Different test elements may be overlapped. This concept allows to get a spatial reconstruction for the unknown defect which is better than the size of the smallest test elements (see [37]). Also, prior information about the unknown defect can be accounted for by properly designing the family of test elements. For instance, if one knows that the unknown defects are horizontally elongated, it would be proper to select horizontally elongated test elements. Three different types of test elements applied in this study are sketched in Fig. 9. Each test element generates a corresponding family of test elements, by means of horizontal or vertical translations at pixel level.

The reconstructions of the target defects for the first family of configurations, the "canonical" configurations of Fig. 5, are showed in Figs. 10–12. Specifically, Figs. 10–12 showed the result of a Monte Carlo study, where the imaging process was repeated on each individual target of Fig. 5, for 1000 different realizations of the noise process. Final results are presented in a gray scale proportional to $\gamma = \text{score}/1000$, where "score" is the number of times a specific pixel is recognized as part of the defect. Therefore, γ assumes values between 0 and 1. A darker pixel (γ closer to 1) is recognized as more likely to be part of the unknown defect, whereas a lighter pixel (γ closer to 0) is recognized as more likely to be external to the unknown defect.

While all three reconstructions are satisfactory, we emphasize the following.

1) With smaller test elements, more details of the unknown defect can be represented. However, as the noise level increases, more errors are expected, as is the case for the reconstructions obtained with the 2×2 test elements.
2) The combination of reconstructions from different families of test elements, is a key for more accurate reconstructions. For instance, results of Fig. 10 demonstrate that the union of the reconstructions achieved with 2×4 and 4×2 test elements are more accurate than the reconstructions obtained by means of any individual family of test elements (either the 2×2, or the 2×4 or the 4×2 family, in our examples).
3) When the test elements are not compatible with the unknown defect, i.e., they are too large, the reconstruction is empty, up to a certain noise level, as shown in Fig. 12. This result demonstrates that if the test elements are too large, relative to the defect size, V may be approximately retrieved only if the noise level increases. The increase in the noise level can be carried out by introducing a synthetic noise.

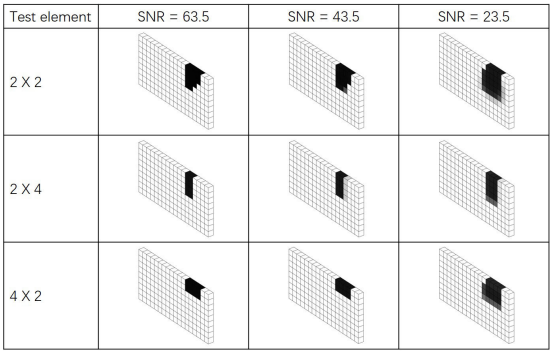

Fig. 10. Reconstruction of defect 1 (surface defect) with various noise level and test elements.

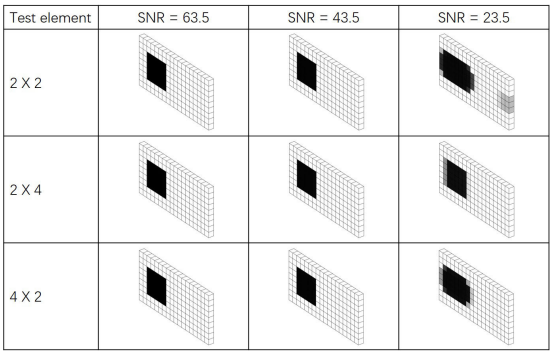

Fig. 11. Reconstruction of defect 2 (buried defect) with various noise level and test elements.

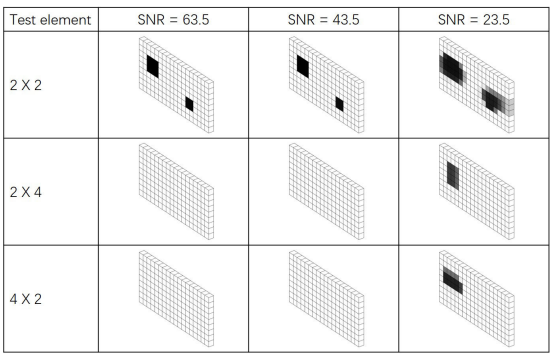

Fig. 12. Reconstruction of defect 3 (interacting defects) with various noise level and test elements.

The reconstructions of the target defects for the second family of configurations, the "complex" configurations of Fig. 6, are shown in Fig. 13. The reconstructions at different noise levels (see top row of Fig. 13) show that retrieving

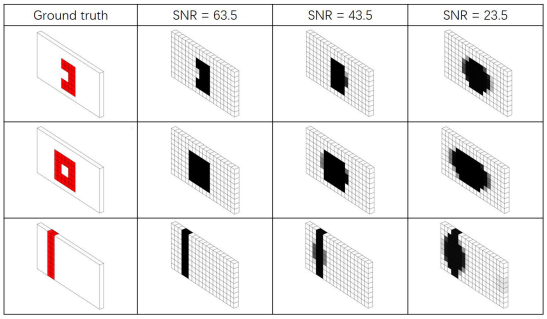

Fig. 13. Reconstruction of the complex defects with various noise levels. Test elements are 2 × 2 squares.

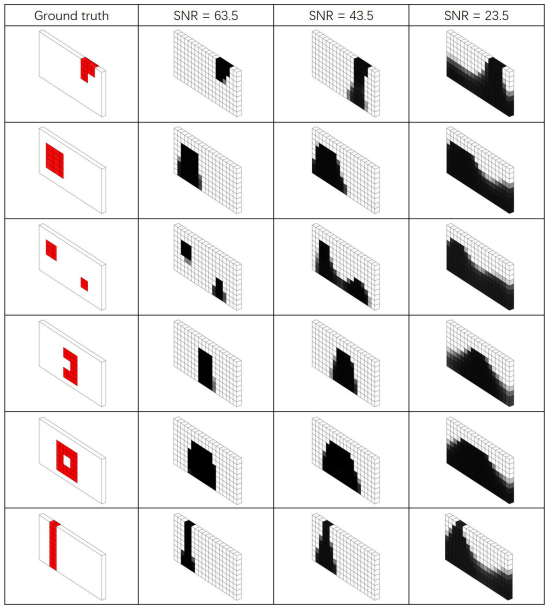

Fig. 14. Reconstructions of the six test defects with the array made by 24 coils placed on the top of the plate. Tests elements are 2 × 2 squares.

a nonconvex defect is challenging and that, as the noise increases, a convexification of the reconstruction occurs. The same convexification of the reconstruction occurs in the case of the nonsimply connected defect in the center row of Fig. 13. This defect is even more challenging because, the hole appears only at a larger SNR, not reported here for the sake of brevity. The third defect, where the ROI is not topologically connected, is retrieved with reasonable accuracy, at several SNR values. We found a degradation of the reconstruction in the innermost parts, at the lower SNR values. This is due to the diffusive nature of the physics underlying ECT, which makes the innermost regions of a material very difficult, if not impossible, to be imaged.

The last set of test examples refer to the impact of the driving system on the quality of the reconstructions. Specifically, we tested: 1) reflection/transmission mode versus pure reflection mode and 2) the impact of the number of elements of the array. The array of Fig. 3, left, combines reflection mode between the 12 elements placed on either the top or the bottom of the plate, and transmission mode between any pair of the elements placed on the two opposite side of the plate.

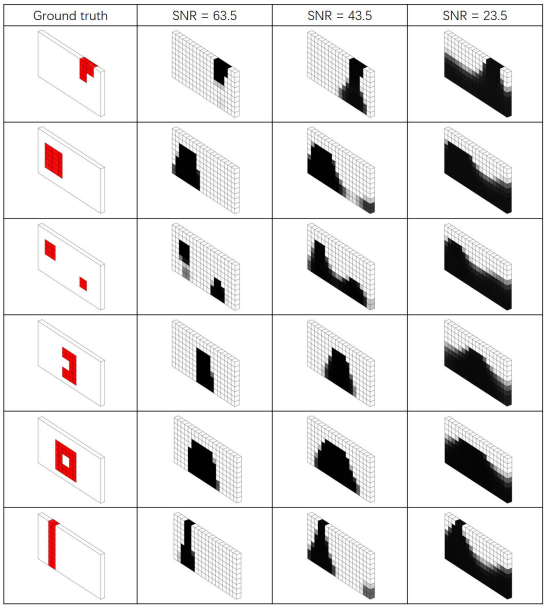

Fig. 15. Reconstructions of the six test defects with the array made by 12 coils placed on the top of the plate. Tests elements are 2 × 2 squares.

When the 24 elements are placed onto the top (bottom) side of the plate (see Fig. 4, left), the coil-to-coil interaction are of reflection type only and, as expected, the performances worsen as seen in Fig. 14. Moreover, the reconstructions worsen progressively in those voxels at increasing distance from the array, as expected from the diffusive nature of the underlying physics. A further degradation appears when one reduces the number of sensors. Fig. 15 showed the reconstruction obtained when using only the 12-element array placed on the top of the plate (see Fig. 4, right). It is worth noting that the worsening in the quality of the reconstruction due to this reduction of the number of elements is less relevant than that due to changing from a reflection/transmission mode to a pure reflection mode, only.

VI. Conclusion

In this article, we developed a MP for the transfer function in ECT, and demonstrated its effectiveness as basis for an imaging method.

Our original contributions are threefold. First, we derived a new operator satisfying the MP, for time-domain eddy current problems. This operator maps the electrical resistivity into a measurable quantity, the transfer function of an array of coils, evaluated on a segment of the real axis. Hence, this operator can be applied to image inhomogeneities in the spatial distribution of the electrical resistivity, via the MP. Second, we proposed a practical approach to measure the transfer function, highlighting all the details to be dealt with. Third, we presented the implementation of the theory in a relevant NDE setup, to estimate the shape of unknown defects in a metal plate. We took advantage of this application case to highlight key features of the method, i.e., the tendency toward convexification of the reconstruction, and the key role of transmission measurements.

Future work of this methodology will include the realization of a prototypical system. With the merit of being nondestructive and nonionizing, our imaging method is an ideal candidate for medical imaging problems, such as imaging of tumors, blood clots, etc.

ACKNOWLEDGMENT

The authors would like to thank Prof. Salvatore Ventre from the University of Cassino and Southern Lazio, Cassino, Italy (salvatore.ventre@unicas.it), for the numerical model used to prepare the examples of Section V.

REFERENCES

[1] D. G. Gisser, D. Isaacson, and J. C. Newell, "Electric current computed tomography and eigenvalues," *SIAM J. Appl. Math.*, vol. 50, no. 6, pp. 1623–1634, Dec. 1990.

[2] A. Tamburrino and G. Rubinacci, "A new non-iterative inversion method for electrical resistance tomography," *Inverse Problems*, vol. 18, no. 6, pp. 1809–1829, Dec. 2002.

[3] D. Colton and A. Kirsch, "A simple method for solving inverse scattering problems in the resonance region," *Inverse Problems*, vol. 12, no. 4, pp. 383–393, Aug. 1996.

[4] A. Kirsch, "Characterization of the shape of a scattering obstacle using the spectral data of the far field operator," *Inverse Problems*, vol. 14, no. 6, pp. 1489–1512, Dec. 1998.

[5] M. Ikehata, "How to draw a picture of an unknown inclusion from boundary measurements. two mathematical inversion algorithms," *J. Inverse Ill-Posed Problems*, vol. 7, no. 3, pp. 255–272, 1999.

[6] M. Ikehata, "On reconstruction in the inverse conductivity problem with one measurement," *Inverse Problems*, vol. 16, no. 3, pp. 785–793, Jun. 2000.

[7] A. Tamburrino, A. Vento, S. Ventre, and A. Maffucci, "Monotonicity imaging method for flaw detection in aeronautical applications," *Stud. Appl. Electromagn. Mech.*, vol. 41, pp. 284–292, Jan. 2016.

[8] B. Harrach and M. Ullrich, "Resolution guarantees in electrical impedance tomography," *IEEE Trans. Med. Imag.*, vol. 34, no. 7, pp. 1513–1521, Jul. 2015.

[9] A. Tamburrino, G. Rubinacci, M. Soleimani, and W. Lionheart, "Non iterative inversion method for electrical resistance, capacitance and inductance tomography for two phase materials," in *Proc. 3rd World Congr. Ind. Process Tomogr.*, 2003, pp. 233–238.

[10] F. Calvano, G. Rubinacci, and A. Tamburrino, "Fast methods for shape reconstruction in electrical resistance tomography," *NDT E Int.*, vol. 46, pp. 32–40, Mar. 2012.

[11] A. Tamburrino and G. Rubinacci, "Fast methods for quantitative eddy-current tomography of conductive materials," *IEEE Trans. Magn.*, vol. 42, no. 8, pp. 2017–2028, Aug. 2006.

[12] A. Tamburrino, S. Ventre, and G. Rubinacci, "Recent developments of a monotonicity imaging method for magnetic induction tomography in the small skin-depth regime," *Inverse Problems*, vol. 26, no. 7, Jul. 2010, Art. no. 074016.

[13] A. Tamburrino, G. Piscitelli, and Z. Zhou, "The monotonicity principle for magnetic induction tomography," *Inverse Problems*, vol. 37, no. 9, Sep. 2021, Art. no. 095003.

[14] Z. Su, S. Ventre, L. Udpa, and A. Tamburrino, "Monotonicity based imaging method for time-domain eddy current problems," *Inverse Problems*, vol. 33, no. 12, Dec. 2017, Art. no. 125007.

[15] Z. Su, L. Udpa, G. Giovinco, S. Ventre, and A. Tamburrino, "Monotonicity principle in pulsed eddy current testing and its application to defect sizing," in *Proc. Int. Appl. Comput. Electromagn. Soc. Symp. Italy (ACES)*, Mar. 2017, pp. 1–2.

[16] A. Tamburrino, Z. Su, S. Ventre, L. Udpa, and S. Udpa, "Monotonicity based imaging method in time domain eddy current testing," *Stud. Appl. Electromagn. Mech.*, vol. 41, pp. 1–8, Jan. 2016.

[17] A. Tamburrino, L. Barbato, D. Colton, and P. Monk, "Imaging of dielectric objects via monotonicity of the transmission eigenvalues," in *Proc. 12th Int. Conf. Math. Numer. Aspects Wave Propag.*, 2015, pp. 20–24.

[18] B. Harrach, V. Pohjola, and M. Salo, "Dimension bounds in monotonicity methods for the Helmholtz equation," *SIAM J. Math. Anal.*, vol. 51, no. 4, pp. 2995–3019, Jan. 2019.

[19] H. Meftahi, "Uniqueness, Lipschitz stability, and reconstruction for the inverse optical tomography problem," *SIAM J. Math. Anal.*, vol. 53, no. 6, pp. 6326–6354, Jan. 2021.

[20] A. C. Esposito, L. Faella, G. Piscitelli, R. Prakash, and A. Tamburrino, "Monotonicity principle in tomography of nonlinear conducting materials," *Inverse Problems*, vol. 37, no. 4, Apr. 2021, Art. no. 045012.

[21] V. Mottola, A. Corbo Esposito, G. Piscitelli, and A. Tamburrino, "Imaging of nonlinear materials via the monotonicity principle," 2023. [Online]. Available: https://arxiv.org/pdf/2310.02935.pdf

[22] B. Harrach and Y.-H. Lin, "Monotonicity-based inversion of the fractional Schrödinger equation I. Positive potentials," *SIAM J. Math. Anal.*, vol. 51, no. 4, pp. 3092–3111, Jan. 2019.

[23] B. Harrach and M. Ullrich, "Monotonicity-based shape reconstruction in electrical impedance tomography," *SIAM J. Math. Anal.*, vol. 45, no. 6, pp. 3382–3403, Jan. 2013.

[24] A. Maffucci, A. Vento, S. Ventre, and A. Tamburrino, "A novel technique for evaluating the effective permittivity of inhomogeneous interconnects based on the monotonicity property," *IEEE Trans. Compon., Packag., Manuf. Technol.*, vol. 6, no. 9, pp. 1417–1427, Sep. 2016.

[25] M. de Magistris, M. Morozov, G. Rubinacci, A. Tamburrino, and S. Ventre, "Electromagnetic inspection of concrete rebars," *COMPEL Int. J. Comput. Math. Electr. Electron. Eng.*, vol. 26, no. 2, pp. 389–398, Apr. 2007.

[26] G. Rubinacci, A. Tamburrino, and S. Ventre, "Concrete rebars inspection by eddy current testing," *Int. J. Appl. Electromagn. Mech.*, vol. 25, nos. 1–4, pp. 333–339, May 2007.

[27] H. A. Haus and J. R. Melcher, *Electromagnetic Fields and Energy*, vol. 107. Englewood Cliffs, NJ, USA: Prentice-Hall, 1989.

[28] D. J. Hagemaier, *Fundamentals of Eddy Current Testing*. Columbus, OH, USA: The American Society of Nondestructive Testing, 2022.

[29] S. S. Udpa and P. O. Moore, "Electromagnetic testing," in *Nondestructive Testing Handbook*, vol. 5. Columbus, OH, USA: American Society for Nondestructive Testing, 2004.

[30] A. Bossavit, "On the numerical analysis of eddy-current problems," *Comput. Methods Appl. Mech. Eng.*, vol. 27, no. 3, pp. 303–318, Jul. 1981.

[31] R. Albanese and G. Rubinacci, "Integral formulation for 3D eddy-current computation using edge elements," *Proc. Inst. Elect. Eng. Phys. Sci., Meas. Instrum., Manage. Educ.*, vol. 135, no. 7, pp. 457–462, Sep. 1988.

[32] R. Albanese and G. Rubinacci, "Finite element methods for the solution of 3D eddy current problems," *Adv. Imag. Electron Phys.*, vol. 102, pp. 1–86, Jul. 1997.

[33] A. Bossavit, *Computational Electromagnetism: Variational Formulations, Complementarity, Edge Elements*. New York, NY, USA: Academic Press, 1998.

[34] R. Albanese and G. Rubinacci, "Treatment of multiply connected regions in two-component electric vector potentials formulations," *IEEE Trans. Magn.*, vol. 26, no. 2, pp. 650–653, Mar. 1990.

[35] G. Rubinacci and A. Tamburrino, "Automatic treatment of multiply connected regions in integral formulations," *IEEE Trans. Magn.*, vol. 46, no. 8, pp. 2791–2794, Aug. 2010.

[36] S. Ventre et al., "Design of a real-time eddy current tomography system," *IEEE Trans. Magn.*, vol. 53, no. 3, pp. 1–8, Mar. 2017. [Online]. Available: https://www.scopus.com

[37] G. Rubinacci, A. Tamburrino, and S. Ventre, "Regularization and numerical optimization of a fast eddy current imaging method," *IEEE Trans. Magn.*, vol. 42, no. 4, pp. 1179–1182, Apr. 2006.

Zhiyi Su (Member, IEEE) received the B.Eng. and M.Sc. degrees in electrical engineering from Tsinghua University, Beijing, China, in 2011 and 2013, respectively, and the Ph.D. degree in electrical and computer engineering from Michigan State University, East Lansing, MI, USA, in 2018.

From 2018 to 2021, he was a full-time Researcher with the Research and Development Division/Automotive Research Laboratory, Hitachi America, Ltd., Farmington Hills, MI, USA. Dr. Su is currently an Engineering Expert with the Zhejiang Laboratory, Hangzhou, Zhejiang, China. His research interests include inverse problems, electromagnetic imaging, radar and camera fusion, and intelligent computing.

Lalita Udpa (Life Fellow, IEEE) received the Ph.D. degree in electrical engineering from Colorado State University, Fort Collins, CO, USA.

She is currently a University Distinguished Professor with the Department of Electrical and Computer Engineering, Michigan State University, East Lansing, MI, USA. She works primarily with the broad areas of electromagnetic nondestructive evaluation, signal processing, and analysis. Her research interests include various aspects of NDE such as development of computational models for NDE, new sensor designs, signal and image processing, data fusion, and inverse problem solutions.

Dr. Udpa is a Fellow of the American Society of Nondestructive Testing and the Indian Society of Nondestructive Testing.

Antonello Tamburrino (Senior Member, IEEE) received the Laurea (summa cum laude) degree in electronic engineering from the University of Naples Federico II, Naples, Italy, in 1992, and the Ph.D. degree in electronic engineering from the Polytechnic of Turin, Turin, Italy, in 1996.

From 2014 to 2018, he was a Full Professor of Electrical Engineering at the College of Engineering, Michigan State University, East Lansing, MI, USA. Since 2006, he has been a Full Professor of Electrical Engineering at the Department of Electrical and Information Engineering, University of Cassino and Southern Latium, Cassino, Italy. He has authored or coauthored more than 250 papers that have appeared in refereed international journals, books, and proceedings of international conferences, and he is a co-editor of three proceedings. His current research interests include inverse problems, electromagnetic imaging, nondestructive evaluation, computational electromagnetism, plasmonics, and homogenization methods.

Dr. Tamburrino is currently an Editor-in-Chief of the scientific journal *International Journal on Applied Electromagnetics and Mechanics*, a Subject Editor of the scientific journal *NDT and E International*, an Associate Editor of the scientific journal *Nondestructive Testing and Evaluation*, and the Chair of the scientific committee of the *Italian Association for Nondestructive Testing, Monitoring, Diagnostic*.

Open Access funding provided by 'Università degli Studi di Cassino e del Lazio Meridionale' within the CRUI CARE Agreement